ACS Catalysis

Research Article

pubs.acs.org/acscatalysis

Delivering a Modifying Element to Metal Nanoparticles via Support: Pt−Ga Alloying during the Reduction of Pt/Mg(Al,Ga)O_x Catalysts and Its Effects on Propane Dehydrogenation

Evgeniy A. Redekop,[†] Vladimir V. Galvita,*[,†] Hilde Poelman,[†] Vitaliy Bliznuk,[‡] Christophe Detavernier,[§] and Guy B. Marin[†]

[†]Laboratory for Chemical Technology, Ghent University, Technologiepark 914, Ghent B-9052, Belgium

[‡]Department of Materials Science and Engineering, Ghent University, Technologiepark 903, Ghent B-9052, Belgium

[§]CoCooN Research Group, Department of Solid State Sciences, Ghent University, Krijgslaan 281/S1, Ghent 9000, Belgium

Supporting Information

ABSTRACT: The alloying of Pt with Ga delivered from a hydrotalcite-like support was investigated as a strategy to produce bimetallic catalysts for propane dehydrogenation. A series of Pt/Mg(Al,Ga)O_x catalysts (2−3 wt % Pt, Ga/Pt molar ratios between 0 and 10) and a model Pt/Ga_2O_3 catalyst (4 wt % Pt, Ga/Pt molar ratio of 50) were characterized by means of X-ray diffraction (XRD), transmission electron microscopy, and activity measurements (873 K, $W_{cat}/F_{C_3H_8,0}$ = 25 kg_{cat}·s·mol^{-1} and $P_{C_3H_8,0}$ = 5 kPa at a total pressure of 101.3 kPa). XRD patterns taken during temperature-programmed reduction in 5% H_2/He and isothermal reduction/oxidation cycling between 5% H_2/He and 20% O_2/N_2 at 873 K revealed dynamic alloy formation and segregation that depended upon the gas environment and Ga content. Alloying on the Pt/Mg(Al,Ga)O_x catalyst with a Ga/Pt ratio of 2 could not be observed by XRD. For a Ga/Pt ratio of 10, an alloy with a diffraction peak at 40.2° was formed during the initial reduction. After subsequent reduction/oxidation treatments, this catalyst evolved toward a stable periodic cycling between pure Pt and one or more Pt−Ga alloys with characteristic peaks at 40.2° and 46.5°. The exact composition of the Pt−Ga alloy(s) could not be identified. On the model Pt/Ga_2O_3 catalyst, an alloy was formed with the same characteristic peak at 40.2° as on the Ga-rich Pt/Mg(Al,Ga)O_x. In addition, another Pt−Ga alloy appeared on the Pt/Ga_2O_3 catalyst, which was identified as a stoichiometric PtGa phase. These alloys were formed on Pt/Ga_2O_3 at a lower temperature than on Pt/Mg(Al,Ga)O_x and they were stable during the reduction/oxidation cycling. Catalytic activity measurements demonstrated that the formation of Pt−Ga alloys on the Pt/Mg(Al,Ga)O_x sample with a Ga/Pt ratio of 10 and on the Pt/Ga_2O_3 catalyst led to pronounced enhancement of the initial selectivity toward propylene, but lower activity per exposed Pt atom.

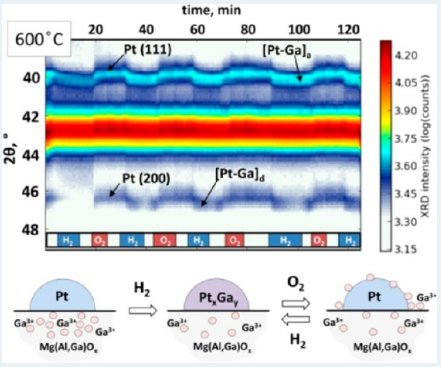

KEYWORDS: *Pt−Ga, bimetallic catalysts, catalyst preparation methods, propane dehydrogenation, in situ XRD*

1. INTRODUCTION

Development of sustainable and efficient catalytic processes requires diverse methods for manipulating catalyst composition and structure, which determine catalysts' performance.[1−5] The active components of many industrial heterogeneous catalysts are composed of supported metal nanoparticles,[6−9] and alloying with additional elements is an important method for manipulating their composition and structure.[10−12] The catalytic behavior of alloyed bimetallic nanoparticles is often markedly different from that of their monometallic counterparts or bulk alloys with equivalent composition due to a combination of geometric and electronic effects.[13−16] The extent of alloying and its effects on catalytic activity crucially depend on the catalyst preparation procedure,[17−19] the nature of the support,[20−22] and the reaction environment.[23,24] Therefore, the influence of these factors must be better understood to fully exploit alloying for rational catalyst design and optimization.

Bimetallic catalysts are mainly prepared by simultaneous or sequential impregnation of the support with constituent metal precursors, followed by calcination and reduction.[25−28] Although such impregnation techniques are widely used in industrial and laboratory practice due to their simplicity and relatively low cost, their capacity to control catalyst composition and structure is far from optimal.[29] This motivates the development of novel techniques for facile catalyst preparation that can selectively deliver modifying elements to supported metal nanoparticles.

Bimetallic catalysts containing Pt are particularly important from a technological perspective because Pt catalysts are heavily

Received: November 4, 2013
Published: April 22, 2014

   dx.doi.org/10.1021/cs500415e | ACS Catal. 2014, 4, 1812−1824

employed in large-scale hydrocarbon processing and other industrially relevant reactions.[1,2,30,31] A specific category of Pt-based catalysts, which includes, but is not limited to, Pt−In,[32,33] Pt−Ge,[34] Pt−Ga,[28,35,36] and most importantly Pt−Sn,[18−20,37,38] has been the subject of intense optimization studies. Such catalysts are increasingly relevant for on-purpose alkane dehydrogenation processes[39,40] and also provide convenient models for elucidating general principles behind alloying effects in catalysis. There is a considerable body of literature devoted to the Pt−Sn catalysts, recently reviewed by Sui et al.;[41] however, less is known about Pt alloying with other metals among the same group.

Several methods based on selective adsorption of precursors have been developed for targeted delivery of a second metal to Pt for alloying. Examples of such methods include in situ reduction of a $Sn(Bu)_4$ precursor preferentially adsorbed on Pt nanoparticles,[18,42] selective deposition of Ru precursors on Pt nanoparticles,[43] and solvated metal atom dispersion (SMAD).[44] Other strategies for selective synthesis of bimetallic nanoparticles utilize the decomposition of stoichiometric bimetallic precursors,[45−47] controlled growth of Pt on bimetallic nanoparticle seeds,[32] colloidal synthesis,[38] atomic layer deposition (ALD),[48] and a range of other synthesis methods. Here, we focus on a recently developed method of catalyst preparation, whereby a second metal is delivered to Pt nanoparticles for alloying via hydrotalcite-like supports.[36,49,50] Unlike some of the aforementioned strategies, this method is simple, inexpensive, and easily scalable. The method involves relatively few synthesis steps, all of which are straightforward to implement and do not require exotic reagents. Moreover, this catalyst synthesis method has a wide range of potential applications outside the context of Pt catalysts, providing a general strategy for controlled delivery of metal precursors to catalyst surfaces.

Magnesium-based hydrotalcites (HTs) are layered materials with the general formula $Mg(Al)O_x$, in which Al^{3+} ions are located in the voids between extended MgO layers. When calcined in air at high temperatures, MgO layers collapse into irregular crystalline structures that expose mostly Mg^{2+}, but also Al^{3+}, sites.[51] These materials have attracted considerable attention as hydrothermally stable nonacidic supports for various catalysts[52] including Pt-based bimetallic catalysts for alkane dehydrogenation.[53,54] In several relevant studies, the interlayer voids of the HT framework were used as delivery vehicles for metal precursors.[49,50,55−57] Sun et al. developed a method for alloying predeposited Pt nanoparticles with Sn, Ga, or In located in the HT framework.[36,54,58] During the first step of this novel catalyst preparation procedure, the corresponding ions are incorporated into the interlayer spaces of the HT framework by coprecipitation with Mg^{2+} from alkaline solutions. After calcination, the resulting high surface area material is used as a support for finely dispersed Pt nanoparticles that are deposited via the classical incipient wet impregnation method. During the next step, this "as-prepared" catalyst is reduced in hydrogen at 923 K to form a bimetallic Pt−M/HT catalyst (M = Sn, Ga, In).

Previous studies established that during the reduction step of this catalyst preparation procedure, M^{3+} ions migrate from the support framework to the surface layer, where they are reduced to metal and alloyed with Pt.[36,49,57−59] In the case of alloying between Pt and Ga, which can form a variety[60,61] of stoichiometric and nonstoichiometric alloys,[62] it was found that the catalytic properties in alkane dehydrogenation are maximized at an optimal Ga/Pt ratio[59] of ∼5.4. It is not clear how the Ga/Pt ratio determines which alloys are formed on the catalyst and at what temperature alloying takes place. It is also important to understand whether bimetallic Pt−Ga nanoparticles are stable in different gas environments, because these catalysts must endure multiple cycles of catalyst regeneration. To address these questions, we have performed in situ X-ray diffraction (XRD) characterization of $Pt/Mg(Al,Ga)O_x$ catalysts during temperature-programmed reduction (TPR), reoxidation, and reduction/oxidation cycling experiments. These experiments were performed for several 2−4 wt % Pt catalysts with variable Ga content in the support, including catalysts supported on HTs with 0, 2, and 10 wt % of Ga and on native Ga_2O_3. The Pt loading of these model catalysts was increased compared to the better dispersed 1 wt % Pt catalysts[36] in order to obtain better XRD signals. XRD results revealed a dynamic picture of Pt−Ga alloying and partial segregation depending on the environment and Ga content. Pt−Ga alloying on the most catalytically relevant material was studied in detail by transmission electron microscopy (TEM) imaging and local energy-dispersive X-ray spectroscopy (EDX) analysis. Furthermore, activity measurements during propane dehydrogenation were used to demonstrate how initial catalytic activity and selectivity of investigated catalysts depend on the extent of Pt−Ga alloying.

2. EXPERIMENTAL SECTION

2.1. Catalyst Preparation. Three HT support materials with 0, 2, and 10 wt % Ga were prepared by coprecipitation from an aqueous solution of Mg (Sigma−Aldrich, 98−102), Al (Sigma−Aldrich, 98.5), and Ga (Sigma−Aldrich, 99.99%) nitrates mixed with a 1.1 mol/L NaOH (Sigma−Aldrich, >98%) solution, as described in Sun et al.[36] The Ga_2O_3 support was prepared by precipitation from an aqueous solution of Ga nitrate (Sigma−Aldrich, 99.99%) mixed with a 1.1 mol/L NaOH solution. After the solution was aged for 24 h at room temperature, all precipitated supports were filtered, dried at 453 K overnight, and then calcined in air at 923 K for 3 h. Next, Pt was deposited on these calcined supports by incipient wet impregnation. Namely, a solution of $Pt(acac)_2$ precursor (Sigma−Aldrich, 99.99%) in toluene (Sigma−Aldrich, 99.9%) was added to the powdered support, followed by toluene evaporation at 453 K and calcination in air at 923 K for 3 h. The resulting "as-prepared" catalysts were reduced in hydrogen during in situ XRD and/or catalytic measurements to form Pt monometallic and/or Pt−Ga bimetallic nanoparticles on their surfaces.

2.2. Catalyst Characterization. The Brunauer−Emmett−Teller (BET) surface areas of calcined supports were determined by N_2 adsorption at 77 K (five point BET method using Gemini Micromeritics) after outgassing each sample at 573 K for 4 h. The crystallographic phases of all supports were confirmed by ex-situ XRD measurements (Siemens Diffractometer Kristalloflex D5000, Cu Kα radiation). The powder patterns were collected in a 2θ range from 10° to 80° with a step of 0.02° and 30 s counting time per angle. XRD patterns of known compounds are referenced by their corresponding number in the Powder Diffraction File (PDF) database.

After Pt deposition, the bulk chemical composition of the as-prepared catalysts was determined by means of inductively coupled plasma atomic emission spectrometry (ICP-AES) (IRIS Advantage system, Thermo Jarrell Ash). The ICP

dx.doi.org/10.1021/cs500415e | ACS Catal. 2014, 4, 1812−1824

samples were mineralized by fusion with sodium peroxide and dissolution in a mixture of HNO_3, HF, and $HClO_4$.

2.3. Microscopy. High-resolution transmission electron microscopy (HRTEM) and bright field (BF) and dark field (DF) scanning transmission electron microscopy (STEM BF) were used for structural analysis. Energy dispersive X-ray spectrometry (EDX) was used for local chemical analysis. These techniques were implemented using a JEOL JEM-2200FS, Cs-corrected microscope operated at 200 kV, which was equipped with a Schottky-type field-emission gun (FEG) and EDX JEOL JED-2300D. All samples were deposited by immersion onto a lacey carbon film on a copper support grid.

2.4. In Situ XRD Measurements. In situ XRD measurements were performed in a home-built reaction chamber housed inside a Bruker-AXS D8 Discover apparatus (Cu Kα radiation of 0.154 nm). The reactor chamber had a Kapton foil window for X-ray transmission. The setup was equipped with a linear detector covering a range of 20° in 2θ with an angular resolution of 0.1°. Pattern acquisition time was approximately 10 s. For each sample, approximately 10 mg of powdered sample was evenly spread on a single crystal Si wafer. Interaction of the catalyst material with the Si wafer was never observed. Before each experiment, the reactor chamber was evacuated to a base pressure of 4 Pa by a rotation pump. Gases were supplied to the reactor chamber from a rig with calibrated mass-flow meters.

A full XRD scan (10° to 65° with a step of 0.02°) was taken at room temperature before and after each TPR, reoxidation, or reduction/oxidation cycling experiment. Samples were cooled in a helium flow to room temperature after high-temperature experiments. For TPR experiments, the sample was resistively heated from room temperature to 923 K at a heating rate of 20 K/min, while flowing 1 mL/s of 5 vol % H_2/He mixture at a total pressure of 101.3 kPa. Reoxidation of the catalyst samples was performed at the same heating rate and final temperature by flowing 1 mL/s of 20 vol % O_2/N_2 mixture at a total pressure of 101.3 kPa. For isothermal reduction/oxidation cycling experiments, the temperature was maintained at 873 K. Cycles consisted of 5−10 min treatments in hydrogen and oxygen mixtures (same flow rates as for TPR and reoxidation), always with 5 min of He purging in between.

It should be noted that peaks in the in situ XRD patterns appeared at slightly shifted angular positions compared to the room temperature scans and tabulated values due to temperature-induced lattice expansion and different sample height. These shifts in peak positions, which are not related to underlying physicochemical processes on the surface, were taken into account during peak assignment using the largest MgO and Ga_2O_3 peaks as references.

2.5. Catalytic Activity Measurements. Activity measurements were performed at atmospheric pressure in a quartz tube microreactor with an internal diameter of 10 mm, which was housed inside an electric furnace (Autochem II 2920, Micromeritics equipped with a TCD detector). Typically, 50 mg of sample was packed between quartz wool plugs. The temperature of the catalyst bed was measured with K-type thermocouples touching the outside and inside of the reactor at the position of the catalyst bed. The inlet gas flow rates were always maintained by means of calibrated Brooks mass flow controllers. The feed and product gas streams were monitored online using a calibrated OmniStar Pfeiffer mass spectrometer (MS). MS signals were recorded for all major fragments of C_3H_8, C_3H_6, C_2H_6, and C_2H_4 species. The fragment at 29 amu was the most intense fragment of C_3H_8, while its contributions for C_2H_6 and C_2H_4 were minor, as verified by additional control experiments. For experiments reported in this paper, the appropriately scaled 29 amu signal (based on the C_3H_8 fragmentation ratios tabulated in the NIST database) was subtracted from 27 to 28 amu signals. The remaining 27−28 amu signals and the 26 amu signal were not significant within experimental error, which led us to conclude that C_2 formation is negligible in our experiments. The 41 amu signal was used to follow C_3H_6 while 16 amu signal was used to follow CH_4. Carbon balance with a maximum deviation of 15% was obtained.

The reaction temperature was limited to 873 K because above that temperature the signs of noncatalytic reactions were observed even without a catalytic sample in the reactor. Each measurement progressed through five consecutive cycles, each of which consisted of the following sequence. First, the sample was reduced in 1 mL/s flow of 5% H_2/Ar at 923 K for 0.5 h. Then, the temperature was decreased to 873 K, while purging with He. At 873 K, an activity measurement was conducted for 1.5 h at $W_{cat}/F_{C_3H_8,0}$ = 25 $kg_{cat}\cdot s\cdot mol^{-1}$ and $P_{C_3H_8,0}$ = 5 kPa (1 mL/s of 5 vol % C_3H_8/He mixture at a total pressure of 101.3 kPa). After a purge with helium, 1 mL/s of 20% O_2/He was introduced in order to burn off carbon deposits until the CO_2 signal returned to the baseline. Carbon burnoff was followed by He purging, after which the cycle was repeated. Experiments were repeated three times with fresh sample material in order to obtain standard deviations. The influence of H_2 cofeeding was investigated for the Pt/HT-10Ga catalyst in similar activity measurements with the addition of pure H_2 gas in 1:1 ratio to propane. Additional stability tests were performed for the Pt/HT-10Ga catalyst in the same setup to elucidate the influence of prolonged exposures to the industrially relevant reactive environment. These tests were performed for 2.5 h at 873 K, $W_{cat}/F_{C_3H_8,0}$ = 18 $kg_{ca}t\cdot s\cdot mol^{-1}$, and $P_{C_3H_8,0}$ = 20 kPa at a total pressure of 101.3 kPa.

The site-time yield (Y, $mol\,s^{-1}\cdot mol_{Pt,s}$) was calculated from the difference in the inlet and outlet molar flow rates, as measured relative to an internal standard (Ar) using an online quadrupole mass spectrometer, i.e.,

$$Y_i = (F_{0,i} - F_i)/N_{Pt,s}$$

where F_i, $mol\cdot s^{-1}$, is the molar flow rate of component i, and $N_{Pt,s}$, $mol_{Pt,s}$, is the amount of exposed (surface) Pt atoms in the sample. The yield was normalized on exposed Pt atoms under the assumption that the fraction of exposed Pt atoms (see Table 1) was determined by the most abundant particle size.

3. RESULTS AND DISCUSSION

3.1. Catalyst Characterization. BET surface areas of supports, metal content, and average diameter of Pt nanoparticles are reported in Table 1 for the four catalytic samples used in this study. Sample labels given in this table are used hereafter to reference specific catalysts. The surface area of all HT supports was well developed. The surface area of Ga-free HT supports was somewhat below previously reported values,[54] whereas the surface areas of Ga-substituted HT supports were consistent with those reported in the literature.[36] The surface area of the Ga_2O_3 support was an order of magnitude lower than that of HT supports.

The structures of all supports were confirmed by ex situ XRD after calcination at 923 K prior to Pt deposition. The XRD

dx.doi.org/10.1021/cs500415e | ACS Catal. 2014, 4, 1812−1824

Table 1. Catalyst Properties

catalyst	metal loading, wt % Pt	Ga	Ga/Pt mol	BET area, m^2/g_{cat}	TEM d_{Pt}, nm	Pt fraction exposed[b]
Pt/HT-0Ga	2.2	0	0	150.7 ± 0.5	13.7 ± 1.9[a]	0.06
Pt/HT-2Ga	3.1	2.0	1.8	109.5 ± 0.4	15.4 ± 4.1[a]	0.06
Pt/HT-10Ga	3.0	9.9	9.3	112.5 ± 0.3	4.8 ± 2.1[a]	0.18
Pt/Ga_2O_3	4.0	71.1	51.0	18.0 ± 0.1	1.8 ± 0.2[a]	0.45

[a]One standard deviation from the mean. [b]Fraction of exposed Pt sites was calculated as $0.9/d_{Pt}$, where d_{Pt} is particle diameter in nm.

scans exhibited characteristic patterns of cubic MgO with major sharp peaks at 42.9° and 62.3° as well as minor peaks at 36.9°, 74.7°, and 78.6° 2θ (PDF 00-045-0946). A separate Ga phase was not observed. Some batches of HT supports showed additional small-intensity peaks, which can be attributed to trace amounts of $MgAl_2O_4$ (30.8°, 36.3°) or $NaAlO_2$ (shoulder at 35.0°) spinels. These compounds were formed in small amounts during support synthesis and did not affect the results of this study.

Prior to experiments with the formation of Pt−Ga alloys, it was determined whether Ga^{3+} ions from the supports can be reduced by hydrogen in the absence of Pt nanoparticles. Figure 1A (top) depicts representative XRD patterns of the HT support with 10 wt % Ga taken before reduction in hydrogen and after reduction followed by exposure to air. If Ga from the HT framework would have migrated to the surface and reduce to metallic form in the hydrogen environment, it would have remained on the surface as Ga_2O_3 after exposure to air. The absence of any changes in the XRD pattern after reduction suggests that either Ga^{3+} ions from the HT framework could not be reduced without Pt nanoparticles, or the reduced and subsequently oxidized Ga did not form Ga_2O_3 domains large enough to produce an XRD pattern. Likewise, no changes were observed in XRD patterns of other supports after reduction (not shown), including the native Ga_2O_3. These results are in agreement with the literature that has suggested that Pt nanoparticles play a crucial role in the reduction of a modifying element from the HT framework.[35,36,63] Most probably, Pt nanoparticles dissociate molecular hydrogen and make it available for reduction of a modifying element from the support.[64]

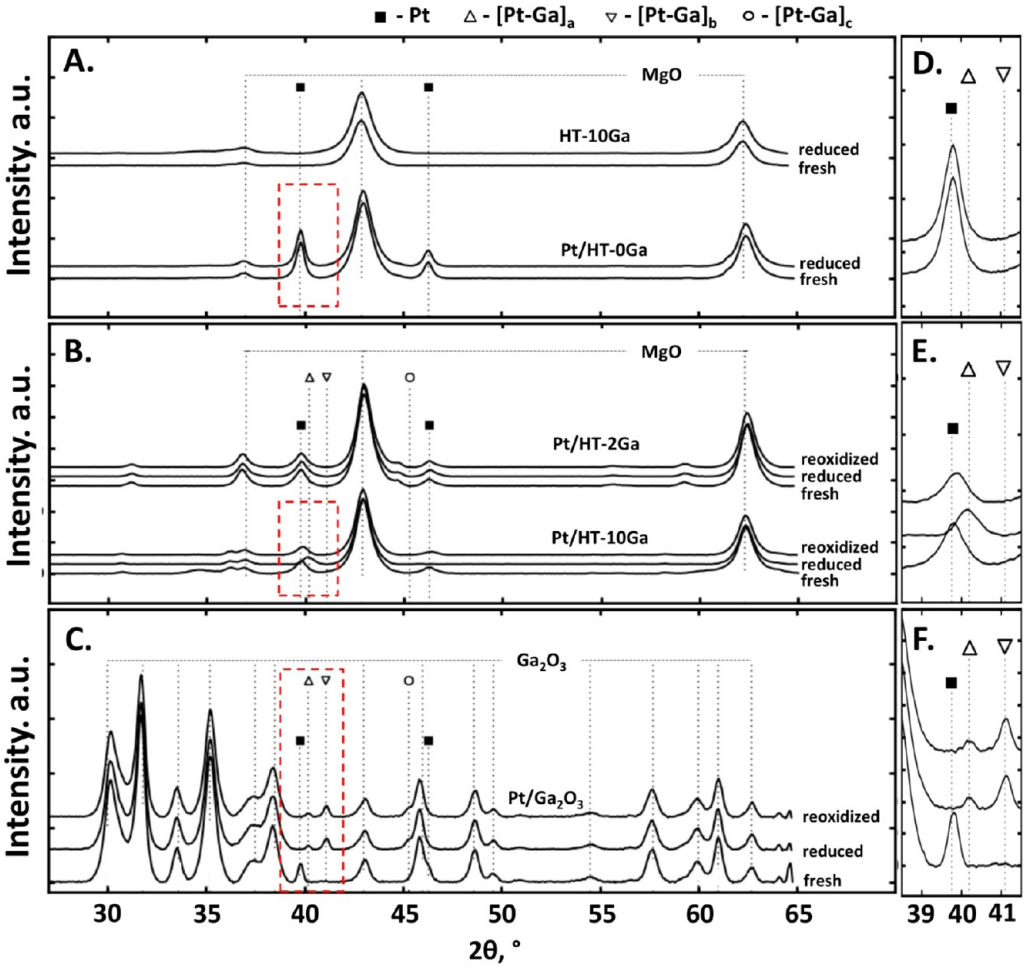

Figure 1. Full XRD scans before and after TPR/reoxidation experiments. (A) Fresh and reduced HT-10Ga support without Pt nanoparticles (top) and Pt/HT-0Ga (bottom). B) Pt/HT-2Ga (top) and Pt/HT-10Ga (bottom) catalysts before and after reduction, as well as after reoxidation. C) Pt/Ga_2O_3 catalyst before and after reduction, as well as after reoxidation. Parts of the XRD patterns that are most relevant to Pt−Ga alloying (dashed rectangles) are shown in more detail in panels D, E, and F. The legend for indicated peak positions is shown at the top of the figure.

dx.doi.org/10.1021/cs500415e | ACS Catal. 2014, 4, 1812−1824

A freshly prepared catalyst without Ga, i.e., Pt/HT-0Ga, was also subjected to a reduction treatment to exclude possible changes not related to Pt−Ga alloying. This control catalyst exhibited characteristic XRD peaks of metallic Pt (PDF 00-004-0802) located at 39.8° (111) and 46.2° (200), as shown in the bottom part of Figure 1A,D. As expected, no changes in the XRD pattern were observed upon reduction of this catalyst without Ga. Because no significant changes related to the main crystallographic phases of support materials have been observed in our experiments, further discussion is focused on Pt and Pt−Ga alloy peaks.

A series of catalysts prepared by Pt deposition onto aforementioned supports spanned a wide range of Ga/Pt ratios (see ICP results in Table 1), providing examples of (relatively) Ga-rich (Ga/Pt ≥ 5) as well as Ga-poor (Ga/Pt ≤ 5) samples. The fresh, reduced, and reoxidized forms of Ga-containing catalysts were characterized with ex situ XRD to elucidate the structure and stability of Pt−Ga alloys. The top part of Figure 1B depicts the patterns of the Pt/HT-2Ga catalyst before reduction, after reduction in hydrogen, and after reoxidation. All three patterns of this Ga-poor catalyst were very similar, indicating that even if Pt−Ga alloying did occur, it did not affect the crystal lattice of XRD-relevant Pt nanoparticles significantly. It should be noted that only Pt nanoparticles above 3 nm contribute to the XRD signal and that alloying of smaller nanoparticles may have occurred without affecting the XRD pattern.

In contrast, XRD patterns of the more Ga-rich Pt/HT-10Ga catalyst exhibited pronounced changes in Pt peaks, as evident from the bottom part of Figure 1B and from Figure 1E. Namely, the intensity of Pt peaks at 39.8° and 46.2° decreased, and a new peak appeared at 40.2°. Henceforth, the latter peak is referred to as [Pt−Ga]a alloy peak. After reoxidation, the intensity of Pt peaks (39.8° and 46.2°) was restored, and the [Pt−Ga]a peak disappeared. These changes can be assigned to the formation of a Pt−Ga alloy with a characteristic peak at 40.2° upon reduction and its decomposition upon reoxidation. The reference patterns of several relatively Pt-rich bulk Pt−Ga alloys exhibit major characteristic peaks slightly above 40°, including Pt_5Ga_3 (221) tabulated at 40.1° (PDF 03-065-7404), Pt_2Ga (112) tabulated at 40.4° (PDF 03-065-4771), and Pt_3Ga (202) tabulated at 40.1° (PDF 03-065-1665). The $[Pt−Ga]_a$ peak can also be assigned to a Pt-rich nonstoichiometric solid solution of Ga in Pt lattice. More specific assessments of bimetallic compositions based on a single peak and without additional data would be speculative.

Even more pronounced changes occurred upon reduction and reoxidation of the model Pt/Ga_2O_3 catalyst with the highest Ga/Pt ratio (Figure 1C,F). The fresh pattern confirmed the presence of multiple characteristic Ga_2O_3 peaks and metallic Pt peaks, although the 46.2° Pt peak was obstructed by Ga_2O_3 peaks. The pattern taken after reduction revealed changes in Pt peaks consistent with Pt−Ga alloying. The peak at 39.8° disappeared, and three new peaks appeared at 40.2° ($[Pt−Ga]_a$), 41.1° ($[Pt−Ga]_b$), and 45.3° ($[Pt−Ga]_c$). The latter peak overlapped with a nearby Ga_2O_3 peak and thus appeared only as a shoulder. These new peaks did not disappear, and the peak at 39.8° was not restored after reoxidation. The $[Pt−Ga]_a$ peak at 40.2° could be equivalent to the one observed after the reduction of the Pt/HT-10Ga catalyst (see Figure 1B,E). The presence of two new $[Pt−Ga]_{b,c}$ peaks at 41.1° and 45.3°, which were not observed after reduction of the less Ga-rich Pt/HT-10Ga catalyst, is consistent with the formation of the PtGa stoichiometric alloy with (210) peak tabulated at 41.2° and (211) peak tabulated at 45.4°.[65,66] Alternatively, but less likely, the $[Pt−Ga]_{b,c}$ peaks could also correspond to the Pt_3Ga (113) peak tabulated at 41.5° (PDF 03-065-1665) and the Pt_5Ga_3 (400) peak tabulated at 45.1° (PDF 03-065-7404), or to nonstoichiometric solutions.

These XRD results confirm the formation of alloyed Pt−Ga nanoparticles and suggest that the extent of Pt−Ga alloying depends on the Ga/Pt ratio in the fresh catalyst. Although no signs of alloying were present in postreduction XRD patterns of Ga-poor catalysts, at least three new diffraction peaks were identified in postreduction XRD patterns of Ga-rich catalysts. An alloy corresponding to one of these peaks (40.2°) was formed on both Pt/HT-10Ga and Pt/Ga_2O_3 catalysts, but it was not stable upon reoxidation in the former case. On the contrary, the alloy with the $[Pt−Ga]_a$ peak and the PtGa alloy formed on the model Pt/Ga_2O_3 catalyst were stable. All Pt−Ga peaks observed in XRD patterns are summarized and labeled in Table 2. This table also contains the fourth Pt−Ga diffraction peak that was observed only during in situ measurements discussed in section 3.3.

Table 2. Identified Diffraction Peaks of Pt−Ga Alloys[a]

diffraction peak (label)	2θ	candidate assignment	Pt/HT-10Ga	Pt/Ga_2O_3
$[Pt−Ga]_a$	40.2°	Pt_5Ga_3 (221) 40.1°, Pt_2Ga (112) 40.4°, Pt_3Ga (202) 40.1°, or solid solution	+	+
$[Pt−Ga]_b$	41.1°	**PtGa (210) 41.2°**, Pt_3Ga (113) 41.5°, or solid solution	−	+
$[Pt−Ga]_c$	45.3°	**PtGa (211) 45.4°**, Pt_5Ga_3 (400) 45.1°, or solid solution	−	+
$[Pt−Ga]_d$	46.5°	Pt_2Ga_3 (111) 46.4°, or solid solution	after second reduction	−

[a]Bold, reference peaks simultaneously matching with experimental data; ±, presence or absence of a peak in XRD patterns of the corresponding sample.

3.2. TEM. TEM micrographs of all as-prepared and spent catalysts revealed the presence of metal nanoparticles with a broad size distribution that was dominated by particles of a certain size, depending on the catalyst (see Table 1). It was expected that Pt nanoparticles were more sintered during catalyst preparation on Ga-rich samples[36] because the presence of Ga decreases the amount of Al sites implicated in Pt anchoring on the surface.[67,68] However, the most Ga-rich HT-10Ga support employed in this study apparently dispersed Pt better than the Ga-free HT and Ga-poor HT-2Ga supports. The dominant particle sizes did not change significantly during high-temperature treatments and reduction/oxidation cycles.

The Pt/HT-10Ga catalyst that exhibited the most pronounced changes of XRD pattern upon alloying was investigated by TEM in more detail. Representative TEM results for the Pt/HT-10Ga catalyst before and after alloying are shown in Figure 2. The STEM BF image in panel A depicts large (>100 nm) and medium ($10 < d < 100$ nm) sized Pt nanoparticles dispersed on the HT support with a characteristic flake-like morphology.[36,54,69] The particles of 5 nm, which constituted the overwhelming majority of particles on this sample, are shown in Figure 2B.

Alloying was confirmed using local and area-averaged EDX analysis of this catalyst before and after reduction. One of the

dx.doi.org/10.1021/cs500415e | ACS Catal. 2014, 4, 1812−1824

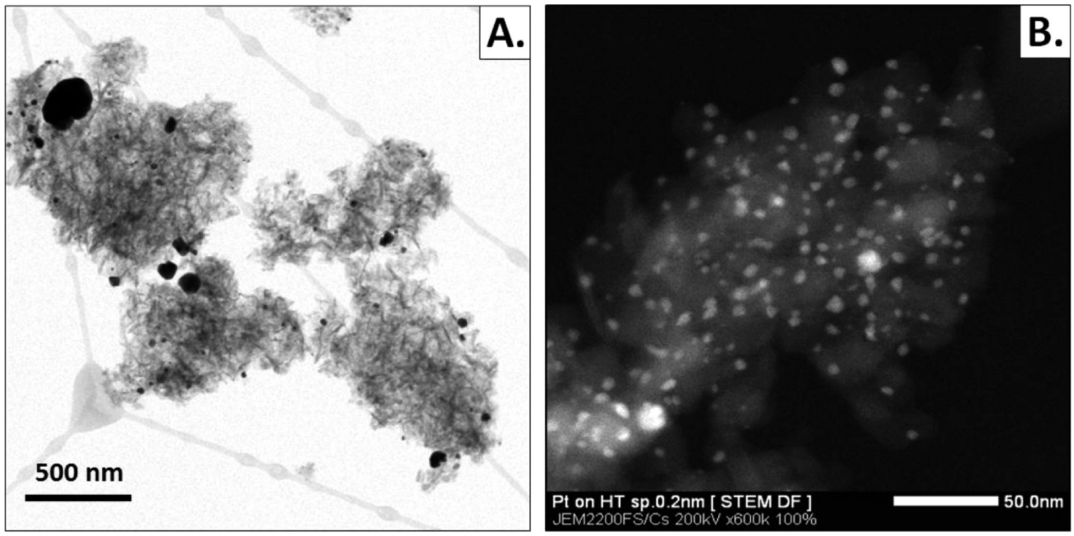

Figure 2. TEM pictures for Pt/HT-10Ga. (A) STEM BF micrographs showing the overall morphology of the Pt/HT-10Ga sample before alloying. (B) STEM DF image of prevalent 5 nm Pt particles after alloying.

50 nm nanoparticles before alloying is shown with higher magnification in Figure 3A. An EDX spectrum taken from the support (inset) confirmed the presence of Al and Ga in the framework of MgO sheets, whereas an EDX spectrum taken from the particle showed mostly pure Pt partially overlapping with HT support. Figure 3B displays a HRTEM image of very small (<2 nm) Pt particles (inside red circles and in other places) before alloying. A characteristic EDX spectrum taken from one of these small Pt nanoparticles (inset) did not exhibit significant Ga content, confirming that "as deposited" Pt is not alloyed with Ga before reduction.

Figure 3C,D depicts TEM images of the same Pt/HT-10Ga sample after it underwent several reduction/oxidation cycles at 873 K, followed by final reduction in hydrogen and cooling in helium. Panel C shows a medium-sized nanoparticle suspended in vacuum and the corresponding EDX spectrum taken from within the entire image. The EDX spectrum confirms the presence of Ga in this alloyed particle. The inset of the same figure depicts a Fourier-transformed (FFT) image of the highlighted rectangular area within the particle's crystalline lattice. The two reflection spots revealed by the Fourier analysis correspond to lattice parameters of 0.276 nm and 0.211−0.215 nm. The former parameter is consistent with the Pt (110) plane (tabulated spacing of 0.277 nm). The latter parameter may correspond to the Pt (111) plane (tabulated spacing of 0.226 nm) with decreased interplanar spacing due to intercalation of Ga into the lattice, in accordance with Vegard's law[70] for bulk nonstoichiometric solid solutions. The decrease in lattice spacing of 0.010−0.016 nm exhibited by Pt (111) planes is quantitatively consistent (according to Bragg's law) with the shift in the XRD pattern of 0.4° exhibited by the Pt (111) peak (39.8° to 40.2°), assuming that the $[Pt-Ga]_a$ diffraction peak corresponds to a solid solution with the same crystal structure as Pt rather than a stoichiometric alloy with a different crystal structure. However, there is no conclusive evidence supporting the formation of a solid solution rather than stoichiometric alloy in this case. Finally, panel D shows very small Pt nanoparticles (<2 nm) after alloying. According to an EDX spectrum taken from one such small particle (lower right inset), the amount of Ga was insignificant compared to Pt. However, the FFT analysis (upper left inset) performed on one of these small particles demonstrated the presence of the Pt (111) plane with decreased lattice spacing (0.210−0.213 nm vs tabulated 0.226 nm).

In addition to the reduced state of the Pt/HT-10Ga catalyst, the reoxidized state was also investigated by TEM to reveal the location of Ga segregated from bimetallic nanoparticles in oxygen environment. The results of this investigation are presented in Figure 4. A typical STEM DF image of a 20 nm Pt nanoparticle is shown in Figure 4A. An EDX line-scan superimposed onto the image reveals the presence of thin Ga-rich shell around the Pt nanoparticle. The same conclusion can be drawn from an EDX elemental mapping of the same region, which is shown in Figure 4B. Ga (green) is clearly localized around Pt (red) particle, while the support contains only trace amounts of Ga and is mostly dominated by Mg (blue).

3.3. Time-Resolved in Situ XRD Measurements.

3.3.1. H_2-TPR. To better understand the formation of Pt−Ga alloys during the reduction process, we performed time-resolved in situ XRD measurements during H_2-TPR of the Pt/HT-10Ga and Pt/Ga_2O_3 samples. Time-resolved XRD patterns of the Pt/HT-10Ga sample are shown in Figure 5A. Two trends corroborating the results of room temperature full XRD scans can be observed in this figure. The Pt peaks at 46.2° and 39.8° gradually decreased from 873 K onward, while a new $[Pt-Ga]_a$ diffraction peak gradually appeared at 40.2°. Both trends can be attributed to the alloying process between Pt nanoparticles and Ga, which migrates from the HT framework upon reduction. Figure 5B depicts the diffraction patterns at 893 K immediately after the start of alloying and at 943 K following alloying completion. The kinetics of the alloying process are represented in Figure 5C by time-dependent integral intensities of the three aforementioned angular positions. The intensities at 39.8° and 46.2° monotonously decrease due to the depletion of monometallic Pt. The intensity at 40.2°, which represents a superposition of the $[Pt-Ga]_a$ peak and portion of the Pt peak at 39.8°, passes through a minimum before increasing toward its final value.

During in situ H_2-TPR of the Pt/Ga_2O_3 sample, the original Pt peak at 39.8° began decreasing from 773 K until it was completely gone at 853 K (Figures 6A,C). A faint peak located

dx.doi.org/10.1021/cs500415e | ACS Catal. 2014, 4, 1812−1824

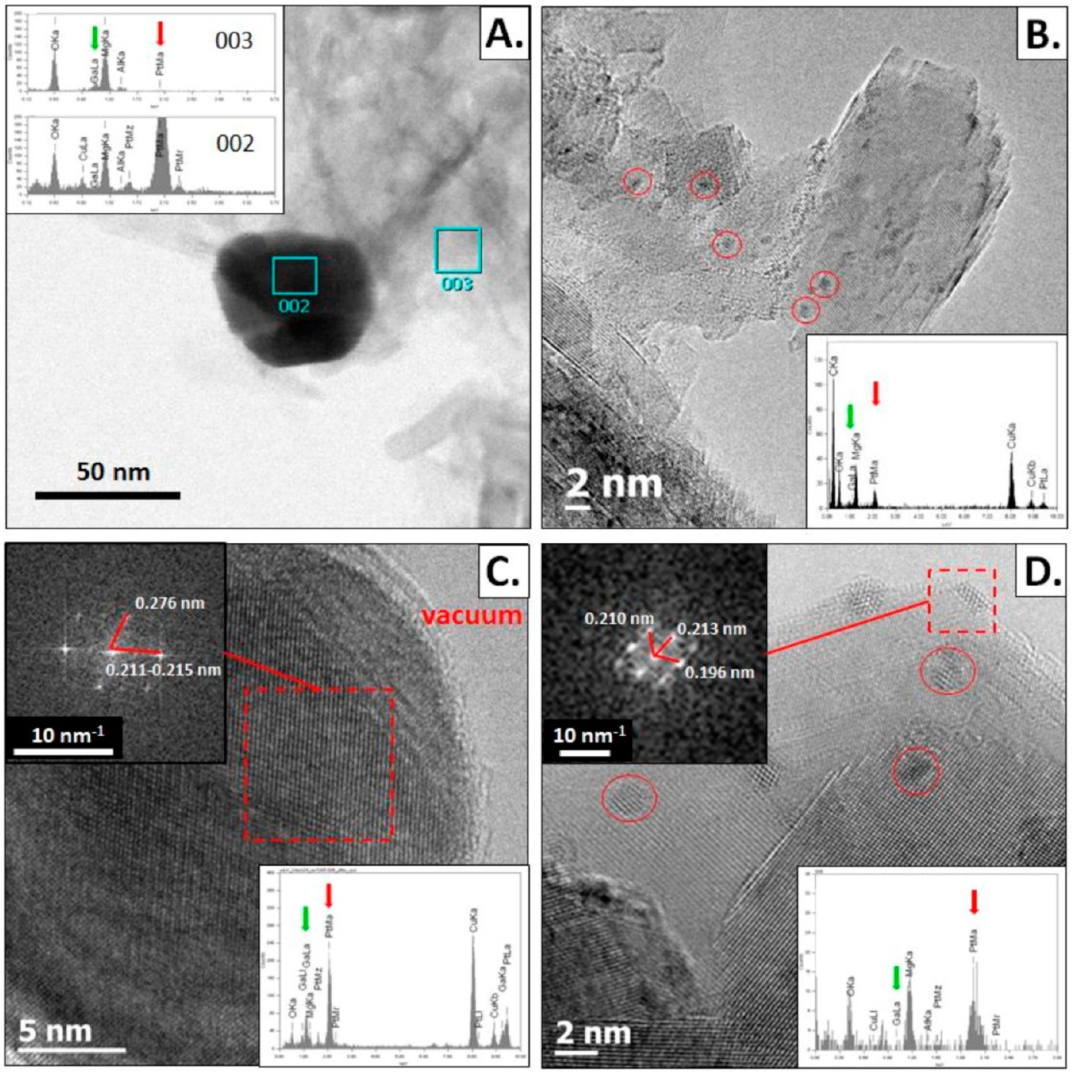

Figure 3. TEM pictures for Pt/HT-10Ga before (A,B) and after (C,D) alloying. (A) STEM BF image of a 50 nm Pt particle and EDX spectra taken from within two highlighted rectangular areas 002 and 003 (arrows indicate the Pt and Ga peaks). (B) HRTEM image of 1−2 nm Pt particles embedded within HT support and an EDX spectrum taken from within one of the highlighted circles. (C) HRTEM image of a medium sized Pt particle suspended in vacuum (after alloying) with an EDX spectrum taken from within the entire frame. The upper-left inset shows FFT of a highlighted rectangular area. (D) HRTEM image of individual 1−2 nm Pt particles (after alloying) with an EDX spectrum taken from one of the particles. The FFT image in the upper left inset was taken from within the highlighted rectangular area.

immediately to the right of the original Pt peak at 39.8° (Figure 6B) can be attributed to the same alloy that was observed at 40.2° ($[Pt-Ga]_a$ peak) after H_2-TPR of the Pt/HT-10Ga catalyst. Concurrently, two new alloy peaks at 41.1° and 45.3° ($[Pt-Ga]_b$ and $[Pt-Ga]_c$) appeared around 813 K and gradually evolved until the temperature reached 853 K. The kinetics of the alloying process are depicted in Figure 6C, where the integral intensities of the Pt (111) peak and the two new $[Pt-Ga]_{b,c}$ peaks are plotted as functions of time. The residual $[Pt-Ga]_a$ peak at 40.2° was not included in this figure due to its weak intensity.

Besides the difference in alloy peaks, a comparison between XRD patterns during H_2-TPR of the Pt/HT-10Ga and Pt/Ga_2O_3 catalysts indicates that Pt−Ga alloying takes place on HT supports at much higher temperature (873 vs 773 K) than on a Ga_2O_3 support. The higher overall activation energy of the alloying process on HT supports probably results from slower Ga migration as well as larger distances that Ga ions must travel before reduction and alloying with Pt.

3.3.2. Isothermal Reduction/Oxidation Cycles. To test the stability of Pt−Ga alloys under different reactive environments, we performed a series of time-resolved in situ XRD measurements during isothermal reduction/oxidation cycling of the Pt/HT-10Ga catalyst at 873 K. A representative set of XRD patterns is plotted in Figure 7A. During the first 4 min, the temperature was raised very quickly to the desired value, resulting in downward expansion shifts of the diffraction peaks present in the pattern. At a stable reaction temperature, the intensity of the entire pattern varied as a function of the gas environment, resulting in periodic intensity variations spanning broad angular regions. However, angular bands at 40−41° and 46−47°, which are relevant to Pt−Ga alloying, exhibited much more pronounced periodic changes. Each of these bands contain two overlapping peaks: a lower-angle peak related to Pt (39.8° and 46.2°) and a higher-angle peak related to Pt−Ga alloys (40.2° and ∼46.5°). To elucidate the dynamic cycling of the catalyst between Pt and Pt−Ga, the integrated intensity of the upper and lower parts of each band are plotted vs time in

dx.doi.org/10.1021/cs500415e | *ACS Catal.* 2014, 4, 1812−1824

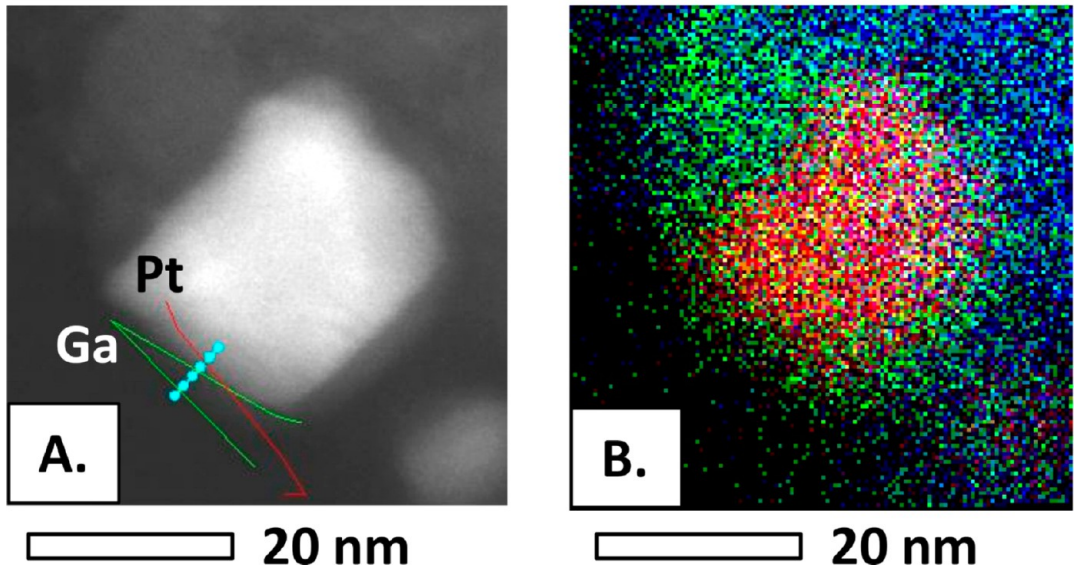

Figure 4. TEM characterization of Pt/HT-10Ga catalyst after reoxidation in oxygen (1 mL/s of 20 vol % O_2/N_2 mixture at a total pressure of 101.3 kPa and 873 K). (A) STEM DF image of a 20 nm Pt particle with superimposed results of an EDX line-scan. Blue dots represent the line of EDX scan, green and red lines represent Ga and Pt content in a.u., respectively. (B) EDX elemental mapping of the same region as in panel A. Blue dots, Mg; green, Ga; red, Pt.

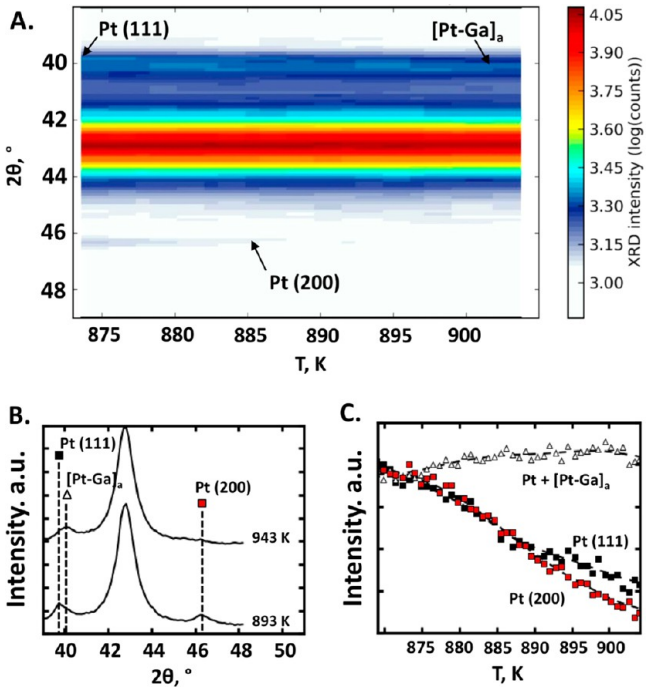

Figure 5. In-situ XRD results during H_2-TPR (20 K/min, 1 mL/s of 5 vol % H_2/He at a total pressure of 101.3 kPa) of the Pt/HT-10Ga catalyst. XRD patterns are aligned with the MgO reference peaks. (A) 2D XRD pattern as a function of temperature. The arrows indicate disappearing Pt peaks at 39.8° and 46.2°, as well as the newly appearing $[Pt{-}Ga]_a$ alloy peak at 40.2°. (B) 2θ sections before and after alloying, which were taken across vertical lines in panel A at 893 and 943 K, respectively. (C) Area under corresponding peaks (integral intensity) vs temperature. The intensity at 40.2° represents Pt and $[Pt{-}Ga]_a$ alloy combined.

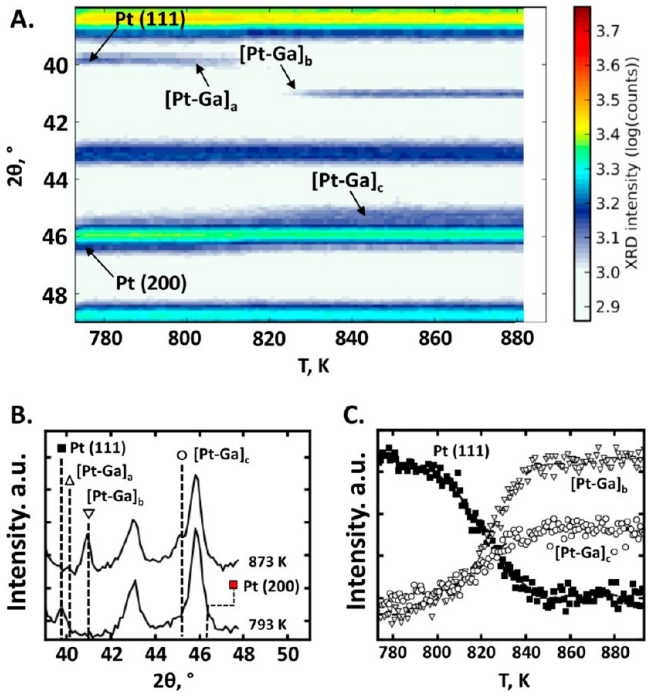

Figure 6. In situ XRD results during H_2-TPR (20 K/min, 1 mL/s of 5 vol % H_2/He at a total pressure of 101.3 kPa) of the model Pt/Ga_2O_3 catalyst. Spectra are aligned with the Ga_2O_3 reference peaks. (A) 2D XRD pattern as a function of temperature. The arrows indicate the disappearing Pt peaks and newly appearing $[Pt{-}Ga]_{a,b,c}$ alloy peaks. (B) 2θ sections before and after alloying, which were taken across vertical lines in panel A at 793 and 873 K, respectively. (C) Area under corresponding peaks (integral intensity) vs temperature.

Figure 7B. The alloy with a characteristic $[Pt{-}Ga]_a$ peak at 40.2° was formed during the first reduction treatment and then exhibited a consistent formation/segregation behavior during subsequent cycles. The intensity of the $[Pt{-}Ga]_a$ peak varied with practically the same periodicity as the intensity of the 39.8° Pt (111) peak. On the contrary, the alloy with a characteristic $[Pt{-}Ga]_d$ peak at 46.5° was not formed during the initial reduction period, although the 46.2° Pt (200) peak completely disappeared. All subsequent reduction/oxidation

dx.doi.org/10.1021/cs500415e | ACS Catal. 2014, 4, 1812−1824

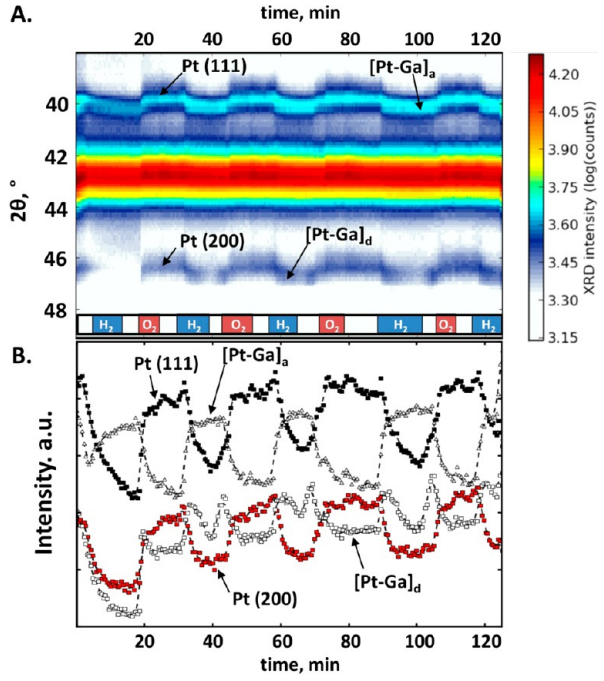

Figure 7. In situ XRD results during reduction/oxidation cycling experiment at 873 K (1 mL/s of alternating 5 vol % H_2/He, He, and 20 vol % O_2/N_2 at a total pressure of 101.3 kPa) with the Pt/HT-10Ga catalyst. Spectra are aligned with the MgO reference peak. (A) 2D XRD pattern as a function of time. The arrows indicate disappearing Pt peaks at 39.8° and 46.2°, as well as newly appearing $[Pt-Ga]_a$ and $[Pt-Ga]_d$ alloy peaks at 40.2° and 46.5°. The sequence of gas environments is shown at the bottom: hydrogen environments are indicated by blue regions, oxygen environments are indicated by red regions, and helium environments in between are left blank. (B) Area under corresponding peaks (integral intensity) vs time.

cycles demonstrated periodic swing between Pt (200) and $[Pt-Ga]_d$ peaks, with the intensity of the latter peak passing through a minimum at the end of every H_2 treatment. The Pt_2Ga_3 (111) peak tabulated at 46.4° (PDF 03-065-1908) is the only reference peak matching the position of this $[Pt-Ga]_d$ diffraction, but it is not likely that such a Ga-rich alloy would be formed on the HT-supported catalyst and not on the model Pt/Ga_2O_3 catalyst (see Figure 1C). It should be noted that neither $[Pt-Ga]_b$ nor $[Pt-Ga]_c$ diffraction peaks were observed for the Pt/HT-10Ga catalyst (see section 3.1).

The first appearance of the $[Pt-Ga]_d$ peak during the second reduction/oxidation cycle suggests that formation of the corresponding alloy requires the presence of Ga in the immediate vicinity of Pt nanoparticles. During the first reduction period, Ga was available for alloying only after migration from the support, and only relatively Ga-poor alloy with the $[Pt-Ga]_a$ diffraction peak could be formed. Upon the first oxidation period, Ga that was already present on the catalyst surface and within bimetallic nanoparticles was segregated as Ga_2O_3. During the second reduction period, the Ga_2O_3 near Pt could be readily reduced and could supply enough Ga for the formation of a Pt−Ga alloy with the $[Pt-Ga]_d$ peak in addition to an alloy with the $[Pt-Ga]_a$ peak.

Passage of the $[Pt-Ga]_d$ peak through a minimum during reductive periods could indicate that the alloy corresponding to this peak is involved in an additional process that is reversible and sequential with respect to initial alloy formation. Assuming, for simplicity, that the $[Pt-Ga]_d$ peak is related to a specific alloy, i.e., independent of the $[Pt-Ga]_a$ peak, such a reversible process may be modeled by the following hydrogen-driven reactions:

$$Pt + Ga \rightarrow [Pt - Ga]_d \quad (s1)$$

$$[Pt - Ga]_d \leftrightarrow [Pt - Ga]_x \quad (s2)$$

where $[Pt-Ga]_x$ is an unidentified alloy with no distinguishable diffraction peaks in the investigated 2θ region. According to this model, the $[Pt-Ga]_d$-related alloy would accumulate at the beginning of the reductive period due to process s1, but would then deplete as a result of process s2 driven by prolonged exposure to hydrogen. Following replacement of hydrogen in the gas phase with He, process s2 would reverse and restore the $[Pt-Ga]_d$-related alloy. Alternatively, the forward direction of reaction s2 may correspond to a dramatic decrease in average particle size, which would also result in decreased XRD intensity of the $[Pt-Ga]_d$ peak. However, it is unlikely that such a coalescence/redispersion process would be sufficiently rapid and fully reversible to explain the observed behavior.

These observations in conjunction with TEM results (Figure 4) clearly demonstrate alloy segregation during reduction/oxidation cycling. Considering the significantly negative Gibbs free energy of Ga_2O_3 formation (−998.3 kJ/mol), it is more likely that segregated Ga forms a Ga_2O_3 phase in the presence of oxygen rather than metallic Ga. Furthermore, this Ga_2O_3 phase appears to be amorphous, because it does not produce characteristic diffraction peaks of crystalline Ga_2O_3. The literature abounds with examples whereby a promoter element segregates from Pt upon oxidation in the form of a separate oxide phase. For example, it was shown that Pt−Sn nanoparticles supported on γ-Al_2O_3[37] and on native SnO_2[71] segregate into Pt and SnO_2 upon oxidative treatments, with SnO_2 decorating the surface of Pt nanoparticles. This phenomenon of Pt decoration with oxide nanoparticles or layers is often implicated in strong metal-support interactions (SMSI).[72,73] Other studies suggested that Sn segregates from the Pt−Sn alloy and spreads over the HT support even during reductive treatments.[69] Similar segregation of a Pt−In alloy into Pt and In_2O_3 phases under an oxidative environment was observed for the $Pt/In_2O_3/Al_2O_3$ catalyst.[33] It is also possible that upon oxidation of the bimetallic catalysts used in this study, mixed Pt−Ga oxides are formed in addition to the Ga_2O_3 phase, according to an XPS study of Pt-assisted migration of structural Ga to the surface of ZSM-5 zeolites.[63]

Overall, the isothermal reduction/oxidation experiment (Figure 7) revealed formation and partial segregation of alloys with at least two diffraction peaks $[Pt-Ga]_{a,d}$. This process evolved over the first two cycles toward a permanent periodic regime oscillating between two consistent states, which are likely to represent the structure of the working catalyst during reductive periods of alkane dehydrogenation and oxidative periods of catalyst regeneration. The environment-dependent mobility of a modifying element on the catalyst surface appears to be a general feature of HT-supported Pt-based bimetallic catalysts,[33,37,63,69] which plays an important role in controlling their catalytic properties.

3.4. Catalyst Activity. The influence of Pt−Ga alloying on the catalytic properties of the Pt/HT catalysts was elucidated by a set of transient activity measurements during propane dehydrogenation. In all activity measurements, the steady-state conversion of propane (6−13%) was significantly lower than the equilibrium conversion of 87% (estimated for the

dx.doi.org/10.1021/cs500415e | ACS Catal. 2014, 4, 1812−1824

initial concentration of 5% and the equilibrium constant[74] of 0.3 atm). Representative results of activity measurements are depicted in Figure 8.

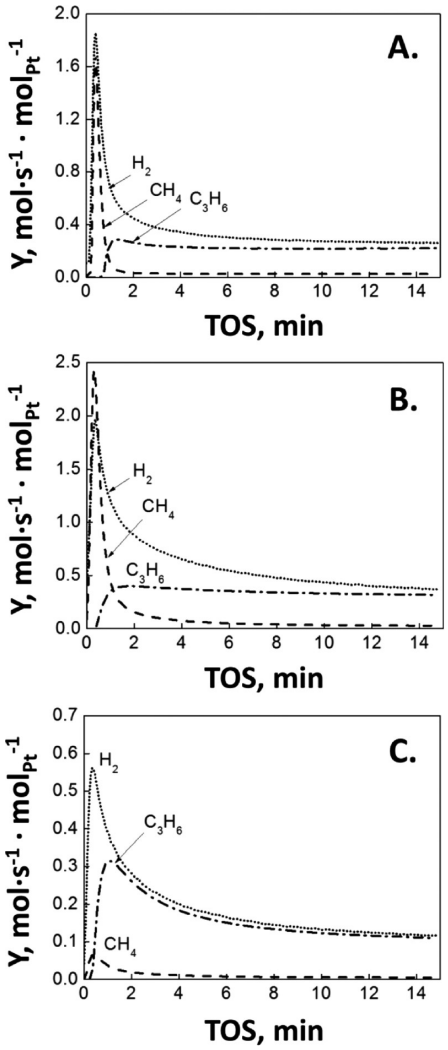

Figure 8. Catalytic propane dehydrogenation at 873 K ($W_{cat}/F_{C_3H_8,0}$ = 25 kg_{cat}·s·mol^{-1} and $P_{C_3H_8,0}$ = 5 kPa at a total pressure of 101.3 kPa): site-time yield (Y, mol·s^{-1}·$mol_{Pt,s}^{-1}$) vs time on stream (TOS, min). (A) Pt/HT-0Ga. (B) Pt/HT-2Ga. (C) Pt/HT-10Ga.

The Pt/HT-0Ga catalyst without Ga was examined in order to establish the catalytic properties of nonalloyed Pt. In Figure 8A, the normalized space-time yields of propylene, hydrogen, and methane, which were the only detectable products, are shown as a function of time-on-stream for this control sample. During the initial minute of the experiment, methane and hydrogen were the main products. After this initial period, when the catalyst adapted to the reaction environment, methane and hydrogen generation sharply declined while propylene generation increased. After passing through a maximum, propylene generation slightly decreased toward a steady-state value of 0.2 mol/s/$mol_{Pt,s}$ with >98% selectivity toward C_3H_6. Beyond 6 min, very little change was observed in space-time yields of all gases. The steady-state hydrogen yield was nearly stoichiometric with respect to propylene yield within the range of experimental error. Experimental data for other catalysts demonstrated similar trends, but there were pronounced differences between the Ga-rich and Ga-poor samples.

The yields of both methane and hydrogen for the Pt/HT-2Ga catalyst (Figure 8B) were somewhat higher than for the Pt/HT-0Ga catalyst. Propylene generation started increasing earlier and reached a slightly higher steady-state value of 0.3 mol/s/$mol_{Pt,s}$. Generally, neither the overall activity nor the ratio of products was altered significantly by the small amounts of Ga present in this sample. The Pt/HT-10Ga catalyst (Figure 8C) exhibited substantially lower activity, with propylene yield reaching 0.1 mol/s/$mol_{Pt,s}$ at steady-state, but higher initial selectivity toward propylene. The peak methane yield was an order-of-magnitude lower than for the previously described samples. An additional activity test with more industrially relevant 20 vol % C_3H_8 feed was conducted for this Pt/HT-10Ga catalyst for 2.5 h at 873 K. No significant deactivation or selectivity loss were observed during this period (see Supporting Information, Figure S2). It should be noted that the final C_3H_6 steady-state selectivity was >98% for both Ga-containing samples. The steady-state propylene yields normalized on exposed Pt atoms (0.1−0.3 mol/s/$mol_{Pt,s}$) where comparable to those previously reported for similar HT-supported Pt−Ga catalysts (0.3 mol/s/$mol_{Pt,s}$ for 0.8 wt % Pt and Ga/Pt molar ratio of 2 under similar reaction conditions).[59]

The model Pt/Ga_2O_3 catalyst with the highest Ga concentration exhibited selectivity trends similar to those of the Pt/HT-10Ga catalyst. However, it was not possible to directly compare the behavior of this model catalyst during the relaxation period to other samples, because the Ga_2O_3 support in the absence of Pt exhibits dehydrogenation activity by itself. Control measurements with bare Ga_2O_3 (see Supporting Information, Figure S6A) demonstrated that the activity of bare Ga_2O_3 was always small and fading quickly during the relaxation period. Hence, the steady-state activity of the Pt/Ga_2O_3 catalyst after the relaxation period (after ca. 10 min on stream) can be attributed solely to the metal nanoparticles. This residual activity was significantly lower than the activity exhibited by all HT-supported Pt catalysts (see Supporting Information, Figure S6B).

The results of activity measurements for the Ga-free Pt/HT-0Ga catalyst may be rationalized in terms of the following three overall reactions:

$$\text{dehydrogenation } C_3H_8 = C_3H_6 + H_2 \quad \text{(r1)}$$

$$\text{deep dehydrogenation } C_3H_8 = 3C + 4H_2 \quad \text{(r2)}$$

$$\text{hydrogenolysis } C_3H_8 + 2H_2 = 3CH_4 \quad \text{(r3)}$$

It has been well established experimentally[75,76] and theoretically[77−79] that deep dehydrogenation (reaction r2) and hydrogenolysis (reaction r3) of hydrocarbons on Pt catalysts are structure-sensitive and promoted by low-coordinated sites, which are typically related to edges, corners, and other defects. Structure sensitivity is also related to the size of Pt ensembles constituting an active site.[80,81] During the initial period of activity measurements reported here, these reactions dominated the catalytic process and led to the formation of primarily hydrogen via deep dehydrogenation and methane via hydrogenolysis. The absence of C_2 products can be explained by their rapid and complete hydrogenolysis into methane. The hydrogenolysis origin of methane was confirmed by cofeeding H_2 with propane (see Figure S4 in the Supporting Information

dx.doi.org/10.1021/cs500415e | ACS Catal. 2014, 4, 1812−1824

for an example of H_2 cofeeding experiment), which showed that in the presence of cofed H_2, methane production increased and was sustained for a longer period of time than in the absence of H_2. Within the first minute on stream, however, the unselective sites were partially or completely blocked by carbon deposits. Passivation of very active low-coordinated Pt sites resulted in increased selectivity toward the less structure-sensitive dehydrogenation reaction (reaction r1), which is also promoted by Pt terraces which remained carbon-free.[82] This coking-assisted transition from low-selectivity period to high-selectivity period is evidenced by a steep sigmoidal shape of C_3H_6 and CH_4 selectivity curves plotted in Figure S3A,B (Supporting Information), respectively, within the first minute of an experiment with the Pt/HT-0Ga catalyst.

Initial selectivity trends (see Figure S3A,B, Supporting Information) for the Pt/HT-2Ga and Pt/HT-10Ga catalysts indicate that the presence of Ga reduces the length of the initial low-selectivity period in comparison with the Ga-free Pt/HT-0Ga catalyst, more sharply so for the Pt/HT-10Ga sample than for the Pt/HT-2Ga sample. Within the simple model outlined above, the observed influence of increased Ga content on the initial activity and selectivity can be explained by a combination of electronic and geometric effects of promoter elements on reactions (1−3). Similarly to Pt−Sn catalysts,[79,83] electron donation from Ga to Pt most likely hinders propylene adsorption on the catalyst and decreases the likelihood of deep dehydrogenation. The nature of geometric effects is less straightforward. Some authors[45,79,83] consider only planar alloy surfaces and attribute the decline in structure sensitive hydrogenolysis and deep dehydrogenation to the decreased size of Pt ensembles on the surface of metal nanoparticles. Other authors[76,84] stress the importance of defect sites as opposed to terrace sites and explain the decline in structure sensitive side reactions by preferential blocking of these defect sites by a promoter element. Both types of geometric effects are likely to contribute to the observed decrease in the overall activity and considerable hindrance of structure sensitive side reactions, especially for the Ga-rich Pt/HT-10Ga and Pt/Ga_2O_3 catalysts. However, activity measurements presented in Figure 8 suggest that hydrogenolysis sites were blocked more readily than deep dehydrogenation sites. This conclusion can be drawn from two observations. First, the H_2/C_3H_6 ratio exhibited by Ga-poor catalysts (Figures 8A,B) remained >1 for a considerable time after the production of methane ceased, suggesting that deep dehydrogenation proceeded longer than hydrogenolysis. Second, Ga-rich catalysts (Figures 8C and S6B, Supporting Information) exhibited more significant reduction in methane generation compared to Ga-poor catalysts than reduction in the initial H_2/C_3H_6 ratio, suggesting that hydrogenolysis sites were blocked by Ga to a larger extent than deep dehydrogenation sites. These subtle differences in the kinetics of hydrogenolysis and deep dehydrogenation can be explained by the difference in structure sensitivity of the two reactions. Hydrogenolysis could be more sensitive to the geometry of low-coordinated defect sites that are the first to be blocked by carbon deposits, even in the absence of Ga, and that are also blocked by Ga upon alloying. Deep dehydrogenation could be less sensitive to the geometry of low-coordinated sites and, therefore, could proceed longer on the Ga-free catalyst, until the size of Pt ensembles was decreased by carbon deposits.

To evaluate catalyst stability, several catalytic cycles were performed that combined periods of propane dehydrogenation followed by periods of catalyst reoxidation, i.e., "coke burn-off". Very little change was observed in the steady-state conversions and yields (see Figure S5, Supporting Information) exhibited by all catalysts from one cycle to the next, while the steady-state propylene selectivity remained above 98% after all cycles for all catalysts. The amount of carbon in mol_C/g_{Pt} deposited on the catalyst per reaction cycle (Figure 9) was consistently lower for

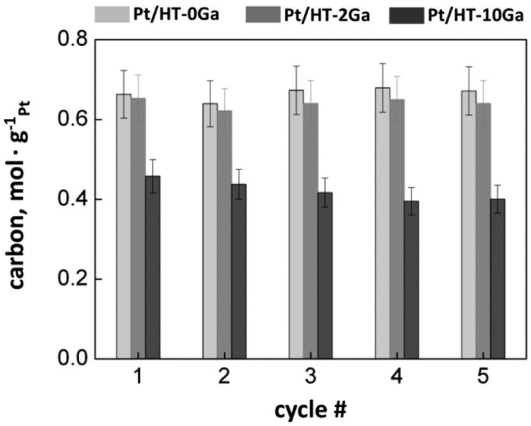

Figure 9. Amount of deposited carbon, $mol \cdot g^{-1}_{Pt}$ per cycle for different catalysts, as determined by CO_2 formation upon reoxidation.

the Pt/HT-10Ga catalyst than for the Pt/HT-0Ga and Pt/HT-2Ga catalysts, with the difference between them growing slightly from one cycle to the next. The molar ratio between accumulated coke and Pt atoms was always much greater than one, but all HT-supported catalysts maintained their steady-state activity. This suggests that only a fraction of active sites were deactivated by coke at the end of every reaction cycle. Most probably, the low-coordinated sites responsible for the initial nonselective period of activity measurements were coked first, while the remaining carbon deposits accounting for $mol_C/mol_{Pt} \gg 1$ were transferred to the support. This explanation is consistent with recent findings providing conclusive TEM evidence of coke transfer from monometallic Pt nanoparticles onto MgO support.[85] Promoter elements were shown to further enhance this coke transfer.[86,87]

4. CONCLUSIONS

The alloying of Pt and Ga, the latter being supplied from Ga-substituted HT support, was studied by in situ XRD and TEM. There was a pronounced difference between the behavior of samples with different Ga concentration upon reduction in hydrogen. Alloy formation on the catalyst with a Ga/Pt molar ratio of 2 was undetectable by XRD analysis. Conversely, XRD analysis of the catalyst with a Ga/Pt ratio of 10 showed the formation of a Pt−Ga alloy (or alloys) with diffraction peaks at 40.2° and 46.5°. The incorporation of Ga into Pt particles was also confirmed by local EDX analysis and TEM imaging. We were unable to determine which specific Pt−Ga alloy(s) were formed on this catalyst, how many different alloys were formed, or whether they were distinct stoichiometric phases or nonstoichiometric solid solutions. The formation of metallic Ga not incorporated into alloys with Pt was never observed even under reductive conditions, suggesting that this new method of Ga delivery to Pt via HT supports is selective. On the Pt/Ga_2O_3 model catalyst, the same diffraction peak at 40.2° was detected upon reduction. Moreover, two additional peaks at 41.1° and 45.3° were formed, neither of which was observed

dx.doi.org/10.1021/cs500415e | ACS Catal. 2014, 4, 1812−1824

on the HT-supported catalysts. These two peaks were assigned to the PtGa stoichiometric alloy.

Ga reduction necessary for alloying started at a much higher temperature on the catalyst with a Ga/Pt ratio of 10 than on the model Pt/Ga_2O_3 catalyst (873 K vs 773 K). The alloy on the former catalyst with an XRD peak at 40.2° was not stable under reduction/oxidation cycling, and significant partially reversible segregation was observed during oxidation periods. Formation of the alloy with the 40.2° peak was observed during the first reduction/oxidation cycle, whereas formation of the alloy with the 46.5° peak was observed only during subsequent cycles. We propose that the initial cycle was necessary for the accumulation of sufficient Ga on the catalyst surface for formation of a more Ga-rich alloy.

Activity measurements indicated that Ga-rich catalysts with Ga/Pt ratios >2 were less active but considerably more selective during the initial minutes of propane dehydrogenation and were less prone to coking than Ga-free and Ga-poor catalysts. Their activity and coking rates were not significantly affected by reaction/regeneration cycling.

Overall, we have demonstrated that after several reduction/oxidation cycles, the investigated HT-supported catalysts evolved toward a permanent periodic regime involving completely reversible Pt−Ga alloying and segregation. These findings will contribute to further optimization of catalysts used for propane dehydrogenation and to further development of the novel method for delivering alloying elements to metal nanoparticles via HT supports.

■ ASSOCIATED CONTENT

Supporting Information

Figures showing the representative calculation of the particle size distribution (Pt/HT-0Ga catalyst), prolonged stability test conducted for Pt/HT-10Ga catalyst under industrially relevant operating conditions for 2.5 h, influence of hydrogen on propylene and methane yields, propylene yield per cycle for different catalysts, and propylene yield per mol of bulk Ga_2O_3 ($mol \cdot s^{-1} \cdot mol_{Ga_2O_3}^{-1}$) as a function of time for the Pt/Ga_2O_3 catalyst and bare Ga_2O_3 catalyst. This material is available free of charge via the Internet at http://pubs.acs.org.

■ AUTHOR INFORMATION

Corresponding Author

*V. V. Galvita. E-mail: Vladimir.Galvita@UGent.be.

Notes

The authors declare no competing financial interest.

■ ACKNOWLEDGMENTS

E.A.R. acknowledges the Marie Curie International Incoming Fellowship granted by the European Commission (Grant Agreement No. 301703). The authors acknowledge the Long Term Structural Methusalem Funding by the Flemish Government, funding provided by the Fund for Scientific Research Flanders (FWO), and the Interuniversity Attraction Poles Programme P7/05 - Belgian State − Belgian Science Policy. The authors also express their gratitude to Olivier Janssens for performing ex situ XRD characterization.

■ REFERENCES

(1) Bond, G. C. *Heterogeneous catalysis: principles and applications*, 2nd ed.; Clarendon Press: New York, 1987.
(2) Boudart, M.; Davis, B. H; Heinemann, H. In *Introduction, in Handbook of Heterogeneous Catalysis*; Ertl, G., Knözinger, H., Weitkamp, J., Eds.; Wiley-VCH: Weinheim, Germany, 2008.
(3) Christensen, C. H.; Norskov, J. K. *J. Chem. Phys.* **2008**, *128*, 182503−182503−8.
(4) Vlachos, D. G.; Caratzoulas, S. *Chem. Eng. Sci.* **2010**, *65*, 18−29.
(5) Zaera, F. *Chem. Soc. Rev.* **2013**, *42*, 2746−2762.
(6) Sachtler, W. M. H.; Schulz-Ekloff, G.; Ernst, S.; Friplat, J. J.; Tanabe, K.; Hattori, H.; Le Page, J. F.; Baerns, M.; Körting, E. In *Preparation of Solid Catalysts, in Handbook of Heterogeneous Catalysis*; Ertl, G., Knözinger, H., Weitkamp, J., Eds.; Wiley-VCH: Weinheim, Germany, 2008.
(7) Chorkendorff, I.; Niemantsverdriet, J. W. *Concepts of Modern Catalysis and Kinetics*; Wiley-VCH: Weinheim, Germany, 2007.
(8) Cuenya, B. R. *Thin Solid Films* **2010**, *518*, 3127−3150.
(9) Schauermann, S.; Nilius, N.; Shaikhutdinov, S.; Freund, H.-J. *Acc. Chem. Res.* **2013**, *46*, 1673−1681.
(10) Besenbacher, F.; Chorkendorff, I.; Clausen, B. S.; Hammer, B.; Molenbroek, A. M.; Nørskov, J. K.; Stensgaard, I. *Science* **1998**, *279*, 1913−1915.
(11) Ponec, V. *Appl. Catal., A* **2001**, *222*, 31−45.
(12) Greeley, J.; Mavrikakis, M. *Nat. Mater.* **2004**, *3*, 810−815.
(13) Toolenaar, F. J. C. M.; Stoop, F.; Ponec, V. *J. Catal.* **1983**, *82*, 1−12.
(14) Ferrando, R.; Jellinek, J.; Johnston, R. L. *Chem. Rev.* **2008**, *108*, 845−910.
(15) Uzio, D.; Berhault, G. *Catal. Rev.* **2010**, *52*, 106−131.
(16) Singh, A. K.; Xu, Q. *ChemCatChem.* **2013**, *5*, 652−676.
(17) Akporiaye, D.; Jensen, S. F.; Olsbye, U.; Rohr, F.; Rytter, E.; Rønnekleiv, M.; Spjelkavik, A. I. *Ind. Eng. Chem. Res.* **2001**, *40*, 4741−4748.
(18) Siri, G. J.; Ramallo-Lopez, J. M.; Casella, M. L.; Fierro, J. L. G.; Requejo, F. G.; Ferretti, O. A. *Appl. Catal., A* **2005**, *278*, 239−249.
(19) Roman-Martinez, M. C.; Macia-Agullo, J. A.; Vilella, I. M. J.; Cazorla-Amoros, D.; Yamashita, H. *J. Phys. Chem. C* **2007**, *111*, 4710−4716.
(20) Barias, O. A.; Holmen, A.; Blekkan, E. A. *J. Catal.* **1996**, *158*, 1−12.
(21) Wunder, R. W.; Phillips, J. *J. Phys. Chem.* **1996**, *100*, 14430−14436.
(22) Yang, L.; Shan, S.; Loukrakpam, R.; Petkov, V.; Ren, Y.; Wanjala, B. N.; Engelhard, M. H.; Luo, J.; Yin, J.; Chen, Y.; Zhong, C.-J. *J. Am. Chem. Soc.* **2012**, *134*, 15048−15060.
(23) Tao, F. (Feng); Zhang, S.; Nguyen, L.; Zhang, X. *Chem. Soc. Rev.* **2012**, *41*, 7980.
(24) Zafeiratos, S.; Piccinin, S.; Teschner, D. *Catal. Sci. Technol.* **2012**, *2*, 1787−1801.
(25) Acres, G. J. K.; Bird, A. J.; Jenkins, J. W.; King, F. The design and preparation of supported catalysts. In *Catalysis*, Vol. 4; Kemball, C., Dowden, D. A., Eds.; RCS Publishing: London, 1981.
(26) Komiyama, M. *Catal. Rev.* **1985**, *27*, 341−372.
(27) Campanati, M.; Fornasari, G.; Vaccari, A. *Catal. Today* **2003**, *77*, 299−314.
(28) Homs, N.; Llorca, J.; Riera, M.; Jolis, J.; Fierro, J.-L. G.; Sales, J.; de la Piscina, P. R. *J. Mol. Catal. A: Chem.* **2003**, *200*, 251−259.
(29) Stair, P. C. *J. Chem. Phys.* **2008**, *128*, 182507−182507−4.
(30) Chen, A.; Holt-Hindle, P. *Chem. Rev.* **2010**, *110*, 3767−3804.
(31) Yu, W.; Porosoff, M. D.; Chen, J. G. *Chem. Rev.* **2012**, *112*, 5780−5817.
(32) Somodi, F.; Werner, S.; Peng, Z.; Getsoian, A. B.; Mlinar, A. N.; Yeo, B. S.; Bell, A. T. *Langmuir* **2012**, *28*, 3345−3349.
(33) Barbosa, R. L.; Papaefthimiou, V.; Law, Y. T.; Teschner, D.; Hävecker, M.; Knop-Gericke, A.; Zapf, R.; Kolb, G.; Schlögl, R.; Zafeiratos, S. *J. Phys. Chem. C* **2013**, *117*, 6143−6150.
(34) Fiddy, S. G.; Newton, M. A.; Campbell, T.; Corker, J. M.; Dent, A. J.; Harvey, I.; Salvini, G.; Turin, S.; Evans, J. *Chem. Commun.* **2001**, 445−446.
(35) Gebauer-Henke, E.; Grams, J.; Szubiakiewicz, E.; Farbotko, J.; Touroude, R.; Rynkowski, J. *J. Catal.* **2007**, *250*, 195−208.

(36) Sun, P.; Siddiqi, G.; Chi, M.; Bell, A. T. *J. Catal.* **2010**, *274*, 192−199.
(37) Uemura, Y.; Inada, Y.; Bando, K. K.; Sasaki, T.; Kamiuchi, N.; Eguchi, K.; Yagishita, A.; Nomura, M.; Tada, M.; Iwasawa, Y. *J. Phys. Chem. C* **2011**, *115*, 5823−5833.
(38) Wang, X.; Altmann, L.; Stover, J.; Zielasek, V.; Bäumer, M.; Al-Shamery, K.; Borchert, H.; Parisi, J.; Kolny-Olesiak, J. *Chem. Mater.* **2013**, *25*, 1400−1407.
(39) Sanfilippo, D. *CATTECH* **2000**, *4*, 56−73.
(40) Vora, B. V. *Top. Catal.* **2012**, *55*, 1297−1308.
(41) Sui, Z.-J.; Zhu, Y.-A.; Li, P.; Zhou, X.-G.; Chen, D. In *Catalysis and Kinetics: Molecular Level Considerations*; Marin, G. B., Eds.; Advances in Chemical Engineering: Vol. *44*; Academic Press: Amsterdam, 2014; pp 61−125.
(42) Santori, G. F.; Casella, M. L.; Siri, G. J.; Adúriz, H. R.; Ferretti, O. A. *Appl. Catal., A* **2000**, *197*, 141−149.
(43) Miura, H. *Catal. Today* **1996**, *28*, 215−221.
(44) Li, Y. X.; Zhang, Y. F.; Klabunde, K. J. *Langmuir* **1988**, *4*, 385−391.
(45) Llorca, J.; Sales, J.; Homs, N.; Fierro, J.; Ramirez de la Piscina, P. *J. Mol. Catal. A: Chem.* **1997**, *118*, 101−111.
(46) Kappenstein, C.; Gue′rin, M.; Lázár, K.; Matusek, K.; Paál, Z. *J. Chem. Soc., Faraday Trans.* **1998**, *94*, 2463−2473.
(47) Small, M. W.; Sanchez, S. I.; Menard, L. D.; Kang, J. H.; Frenkel, A. I.; Nuzzo, R. G. *J. Am. Chem. Soc.* **2011**, *133*, 3582−3591.
(48) Weber, M. J.; Mackus, A. J. M.; Verheijen, M. A.; van der Marel, C.; Kessels, W. M. M. *Chem. Mater.* **2012**, *24*, 2973−2977.
(49) Nagaoka, K.; Jentys, A.; Lercher, J. A. *J. Catal.* **2005**, *229*, 185−196.
(50) Takehira, K. *J. Nat. Gas Chem.* **2009**, *18*, 237−259.
(51) McKenzie, A. L.; Fishel, C. T.; Davis, R. J. *J. Catal.* **1992**, *138*, 547−561.
(52) Tichit, D.; Coq, B. *CATTECH* **2003**, *7*, 206−217.
(53) Virnovskaia, A.; Rytter, E.; Olsbye, U. *Ind. Eng. Chem. Res.* **2008**, *47*, 7167−7177.
(54) Galvita, V.; Siddiqi, G.; Sun, P.; Bell, A. T. *J. Catal.* **2010**, *271*, 209−219.
(55) Basile, F.; Basini, L.; Fornasari, G.; Gazzano, M.; Trifirò, F.; Vaccari, A. *Chem. Commun.* **1996**, 2435−2436.
(56) Ota, A.; Armbrüster, M.; Behrens, M.; Rosenthal, D.; Friedrich, M.; Kasatkin, I.; Girgsdies, F.; Zhang, W.; Wagner, R.; Schlögl, R. *J. Phys. Chem. C* **2011**, *115*, 1368−1374.
(57) Armbruster, M.; Behrens, M.; Cinquini, F.; Fottinger, K.; Grin, Y.; Haghofer, A.; Klotzer, B.; Knop-Gericke, A.; Lorenz, H.; Ota, A.; Penner, S.; Prinz, J.; Rameshan, C.; Révay, Z.; Rosenthal, D.; Rupprechter, G.; Sautet, P.; Schlögl, R.; Shao, L.; Szentmiklósi, L.; Teschner, D.; Torres, D.; Wagner, R.; Widmer, R.; Wowsnick, G. *ChemCatChem.* **2012**, *4*, 1048−1063.
(58) Sun, P.; Siddiqi, G.; Vining, W. C.; Chi, M.; Bell, A. T. *J. Catal.* **2011**, *282*, 165−174.
(59) Siddiqi, G.; Sun, P.; Galvita, V.; Bell, A. T. *J. Catal.* **2010**, *274*, 200−206.
(60) Anres, P.; Gaune-Escard, M.; Bros, J. P. *J. Alloys Compd.* **1996**, *234*, 264−274.
(61) Li, M.; Li, C.; Wang, F.; Zhang, W. *Intermetallics* **2006**, *14*, 826−831.
(62) Hereafter, the term alloy is used collectively for stoichiometric and nonstoichiometric bimetallic compounds.
(63) Melo, L.; Díaz, Y.; Mediavilla, M.; Albornoz, A.; Brito, J. L. *Catal. Lett.* **2004**, *97*, 105−109.
(64) Sermon, P. A.; Bond, G. C. *Catal. Rev.* **1974**, *8*, 211−239.
(65) Bhargava, M. K.; Gadalla, A. A.; Schubert, K. *J. Less Common Met.* **1975**, *42*, 76.
(66) Kim, Y. K.; Baugh, D. A.; Shuh, D. K.; Stanley Williams, R.; Sadwick, L. P.; Wang, K. L. *J. Mater. Res.* **1990**, *5*, 2139−2151.
(67) Kwak, J. H.; Hu, J.; Mei, D.; Yi, C.-W.; Kim, D. H.; Peden, C. H. F.; Allard, L. F.; Szanyi, J. *Science* **2009**, *325*, 1670−1673.
(68) Mei, D.; Kwak, J. H.; Hu, J.; Cho, S. J.; Szanyi, J.; Allard, L. F.; Peden, C. H. F. *J. Phys. Chem. Lett.* **2010**, *1*, 2688−2691.
(69) Virnovskaia, A.; Jørgensen, S.; Hafizovic, J.; Prytz, Ø.; Kleimenov, E.; Hävecker, M.; Bluhm, H.; Knop-Gericke, A.; Schlögl, R.; Olsbye, U. *Surf. Sci.* **2007**, *601*, 30−43.
(70) Denton, A. R.; Ashcroft, N. W. *Phys. Rev. A* **1991**, *43*, 3161−3164.
(71) Kamiuchi, N.; Matsui, T.; Kikuchi, R.; Eguchi, K. *J. Phys. Chem. C* **2007**, *111*, 16470−16476.
(72) Tauster, S. J. *Acc. Chem. Res.* **1987**, *20*, 389−394.
(73) Liu, J. (Jimmy) *ChemCatChem.* **2011**, *3*, 934−948.
(74) Weckhuysen, B. M.; Schoonheydt, R. A. *Catal. Today* **1999**, *51*, 223−232.
(75) Rovik, A. K.; Klitgaard, S. K.; Dahl, S.; Christensen, C. H.; Chorkendorff, I. *Appl. Catal., A* **2009**, *358*, 269−278.
(76) Jones, L. C.; Gordon, M. J. *J. Phys. Chem. C* **2012**, *116*, 23472−23476.
(77) Watwe, R. M.; Cortright, R. D.; Nørskov, J. K.; Dumesic, J. A. *J. Phys. Chem. B* **2000**, *104*, 2299−2310.
(78) Anghel, A. T.; Jenkins, S. J.; Wales, D. J.; King, D. A. *J. Phys. Chem. B* **2006**, *110*, 4147−4156.
(79) Yang, M. L.; Zhu, Y. A.; Fan, C.; Sui, Z. J.; Chen, D.; Zhou, X. G. *Phys. Chem. Chem. Phys.* **2011**, *13*, 3257−3267.
(80) Campbell, C. T.; Campbell, J. M.; Dalton, P. J.; Henn, F. C.; Rodriguez, J. A.; Seimanides, S. G. *J. Phys. Chem.* **1989**, *93*, 806−814.
(81) Ribeiro, F. H.; Bonivardi, A. L.; Somorjai, G. A. *Catal. Lett.* **1994**, *27*, 1−10.
(82) Wu, J.; Peng, Z.; Bell, A. T. *J. Catal.* **2014**, *311*, 161−168.
(83) Nykanen, L.; Honkala, K. *J. Phys. Chem. C* **2011**, *115*, 9578−9586.
(84) Virnovskaia, A.; Morandi, S.; Rytter, E.; Ghiotti, G.; Olsbye, U. *J. Phys. Chem. C* **2007**, *111*, 14732−14742.
(85) Peng, Z.; Somodi, F.; Helveg, S.; Kisielowski, C.; Specht, P.; Bell, A. T. *J. Catal.* **2012**, *286*, 22−29.
(86) Bond, G. C. *Appl. Catal., A* **1997**, *149*, 3−25.
(87) Vu, B. K.; Song, M. B.; Ahn, I. Y.; Suh, Y.-W.; Suh, D. J.; Kim, J. S.; Shin, E. W. *J. Ind. Eng. Chem.* **2011**, *17*, 71−76.